Cite as:

Camara A., Jagadeesh C and Divall S. (2026). Wind–vehicle–bridge interaction and driving safety reliability under skew winds. Engineering Structures, 365: 123243.

Wind-vehicle-bridge interaction and driving safety reliability under skew winds

Alfredo Camara[a], Chetan Jagadeesh[b], Sam Divall[b]

[a]*Department of Continuum Mechanics and Theory of Structures, Universidad Politécnica de Madrid, Calle Profesor Aranguren s/n, 28040 Madrid, Spain.*
[b]*City St George's, University of London, Northampton Square, London EC1V 0HB. United Kingdom.*

Abstract

Wind-induced vehicle accidents on bridges depend not only on mean wind speed but also on turbulence and pavement roughness. Existing wind-vehicle-bridge interaction (W-VBI) studies typically rely on a limited number of stochastic wind and pavement realisations, restricting the quantification of record-to-record variability in driving safety. This study proposes a W-VBI framework that explicitly embeds this variability into the driving safety assessment. Applied to a twin box-girder bridge, the methodology combines stochastic simulations of turbulent wind and pavement profiles with aerodynamic coefficients obtained from wind-tunnel tests, which are used to define wind loads in the coupled W-VBI analysis. Over 85,000 nonlinear simulations are conducted for 11 wind angles, five gust levels, two high-sided vehicles, and speeds from 15-130 km/h. Vehicle overturning, side-slipping, and yawing probabilities are calculated, using bootstrapping techniques to evaluate the statistical stability of the simulations. Results show that wind and pavement randomness induce significant record-to-record variability in vehicle safety, while bootstrapping enables estimation of the minimum number of stochastic records required for statistically stable reliability assessments.

Keywords:

Wind-vehicle-bridge interaction; wind-induced traffic instabilities; record-to-record variability; bridges; skew winds; pavement irregularities

Email address: alfredo.camara@upm.es (Alfredo Camara)

1. Introduction

Wind-induced traffic interruptions and accidents pose a major operational challenge for long-span bridges worldwide [1]. For some of these structures exposed to strong winds, operational restrictions are governed by the driving safety of high-sided vehicles before structural limits of the bridge are reached [2, 3, 4]. Evaluating driving safety requires identifying the wind conditions under which overturning, side-slipping, or loss of control may occur. In long-span systems, this assessment involves a fully coupled wind–vehicle–bridge interaction (W-VBI) problem in which the aerodynamic excitation of the deck, the dynamic response of the bridge, and the vehicle-pavement interaction must be treated in the time-domain.

Early W-VBI studies established semi-analytical formulations that compute wind forces on vehicles and decks from aerodynamic coefficients and solve the coupled equations of motion at each time step [5, 6]. Subsequent developments extended these formulations to fully coupled vehicle-deck motion, typically relying on modal superposition of the bridge response for computational efficiency [7]. Most of the previous works focus on driving safety under crosswinds, showing that lateral vehicle vibrations are dominated by wind loading, whereas vertical vehicle vibrations depend strongly on road roughness [8, 9]. These works underline that both bridge motion and road unevenness may significantly amplify wind-induced vehicle dynamics.

Driving safety is highly sensitive to pavement irregularities, which affect significantly the vehicle-bridge interaction [8]. Road roughness is commonly represented using one-dimensional stationary Gaussian processes, which capture longitudinal correlations but not transverse ones. Many W–VBI studies apply identical profiles to both wheel paths, or do not explicitly report the transverse correlation model used [10, 11]. Similar considerations apply to turbulent wind fields, typically generated as stochastic realisations from target spectra. Yet the number of pavement and wind records employed is often small; for instance, Xu and Guo used five samples [6, 12], and other works used eight [9] or ten records [3]. Camara *et al.* [4] showed that record-to-record variability significantly affects both safety and comfort predictions, underscoring the need for ensemble-based analyses.

Recent studies have broadened the scope of W-VBI by examining aerodynamic interference [13, 14], physics-driven surrogate modelling [15], nonstationary winds [16], wind-rain effects [17], vortex-induced vibrations [18, 19], ice-wind coupling [20], wake flow from upwind bridges [21], and data-driven risk evaluation [22, 23]. However, these works typically rely on a single pavement profile, a single wind history, or unspecified sample sizes, meaning that stochastic dispersion is not reported or assessed. Yang *et al.* [24] has also highlighted the importance of the variability in the wind turbulence and the contact irregularities in vehicle safety assessment, although their probabilistic decoupling framework is limited to railway applications and orthogonal wind conditions. Consequently, despite significant advances in modelling complexity, the literature still lacks a systematic quantification of record-to-record variability and its implications for probabilistic driving safety assessments and traffic management for road bridges under skew winds.

To address this gap, the present study develops a W-VBI framework that explicitly quantifies record-to-record variability induced by stochastic turbulent wind and pavement irregularities, embedding these uncertainties into probabilistic vehicle driving safety assessments under skew wind conditions, for which critical wind curves are established for the first time. Unlike previous studies typically based on a limited number of orthogonal wind or pavement records, the proposed framework enables statistically stable reliability estimates through large-ensemble simulations and bootstrap analysis. The methodology is applied to a conventional double box-girder prestressed concrete bridge under an extensive set of wind conditions, vehicle types, and traffic scenarios. This study contributes a practical framework for incorporating stochastic wind and pavement uncertainties into W-VBI analyses, supporting more statistically robust reliability assessments and wind-related traffic management strategies for large bridges.

2. Methodology

This study proposes a stochastic W-VBI framework to assess the driving safety of high-sided vehicles crossing bridges under turbulent skew winds and pavement irregularities.

The workflow combines pre-processing of stochastic inputs and aerodynamic data, time-domain coupled dynamic simulations, and statistical post-processing of the accident risk indicators. The W-VBI framework has 4 steps described in Fig. 1.

Step 1: Modelling of the bridge and the vibration sources

First, the wind field and the pavement irregularities on the site of the bridge are defined along with the dynamic properties of the structure. This information is included in the matrix containing the relevant vibration mode shapes ($\mathbf{\Phi}$) and the corresponding vibration frequencies (f), obtained from finite element (FE) analysis of the bridge.

Synthetic wind speed records are generated as three-dimensional (3D) pseudo-random turbulent wind fields correlated in time and space, and inclined relative to the deck. To apply Veers' methodology [25] for generating orthogonal wind fields, an auxiliary plane perpendicular to the mean wind is defined following [3]. This Generation Plane (GP) is a vertical plane upwind from the structure, forming an angle β with the vector normal to the structural plane (SP), as shown in Fig. 1(a). The wind field in the GP superimposes the mean speed U onto zero-mean turbulence components, generated at the orthogonal projections of the N_p structural nodes. The generated wind histories preserve the prescribed turbulence intensity, integral length scales, and temporal/spatial correlation structure, enabling realistic simulation of gust events travelling across the bridge deck under skew wind conditions. The hat symbol $\widehat{(\cdot)}$ denotes quantities in the GP: $\widehat{x}$ (across-flow horizontal), $\widehat{y}$ (along-flow), and $\widehat{z}$ (vertical, aligned with SP's z-axis).

Pavement irregularity surfaces are implemented as imposed displacement profiles at the vehicle wheels. Distinct profiles are generated for the leeward and windward wheel lines (r_L and r_W, respectively). These ergodic, stationary Gaussian random processes are based on the target displacement Power Spectral Density (PSD) $G_d(n) = G_d(n_0)(n/n_0)^{-2}$ from ISO 8608 [26] for Road Category A, where n is spatial frequency, n_0 the discontinuity frequency and $G_d(n_0)$ is the road quality parameter. The road profiles r_W (reference) and r_L are separated transversely by the vehicle width ($2b$), with partial correlation governed by: (1) spatial frequency content, and (2) transverse separation. Under isotropic and homogeneous assumptions, profiles are generated via Shinozuka's method [27]:

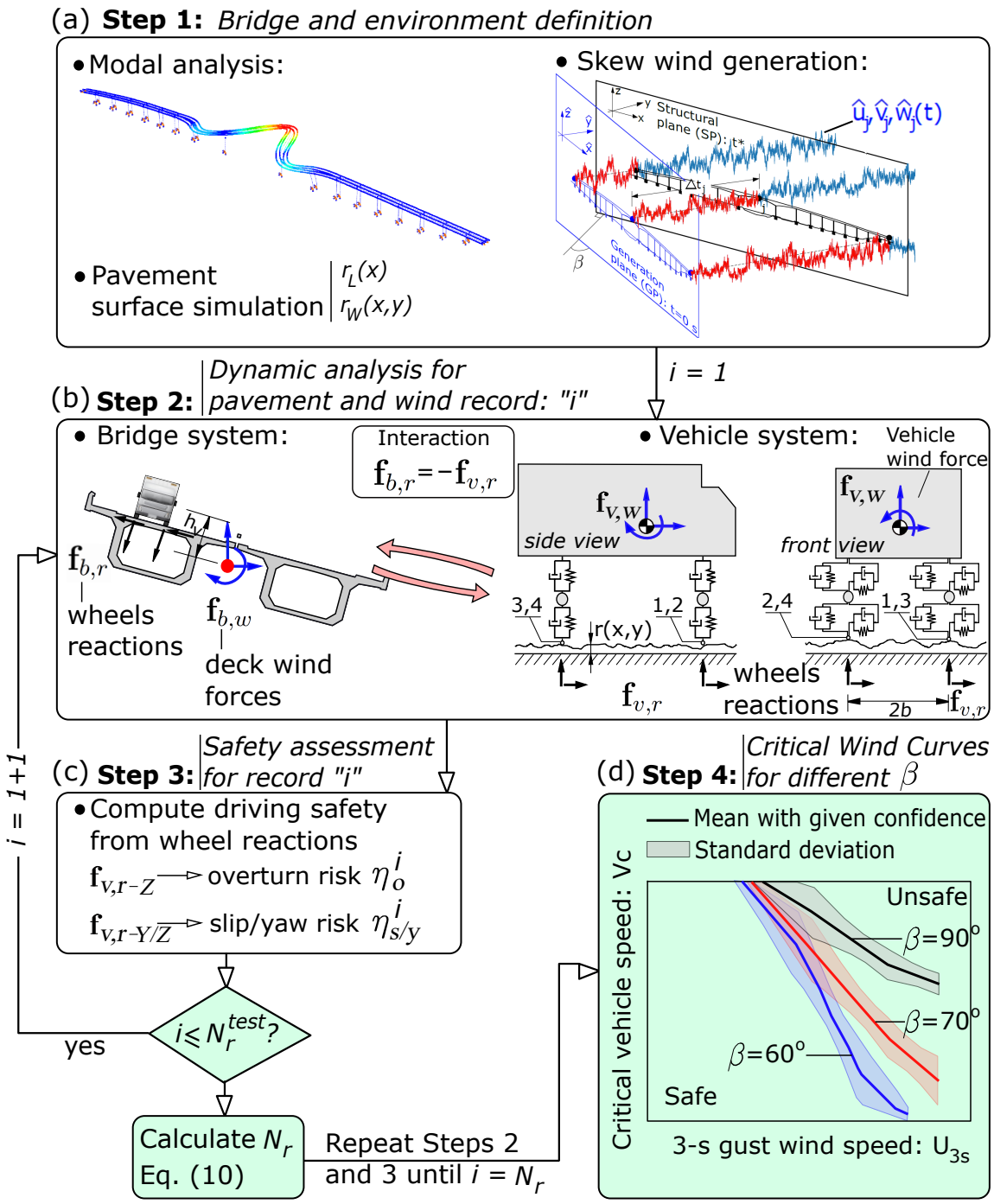

Figure 1: W-VBI framework supporting the driving safety assessment in this work: (a) pre-processing, (b) analysis, (c) post-processing, (d) traffic operation assessment for different wind angles. The novelties in the methodology are highlighted in green.

$$r(x,y) = \sum_{i=1}^{N} \Big[\sqrt{2G_{xy}(n_i)\,\Delta n}\,\cos(2\pi n_i x + \phi_i) + \sqrt{2(G(n_i) - G_{xy}(n_i))\Delta n}\,\cos(2\pi n_i x + \theta_i) \Big], \tag{1}$$

where N is the number of spatial frequencies; Δn is the spatial frequency resolution; G_{xy} is the one-sided cross PSD; ϕ_i and θ_i are independent random phases.

Step 2: Dynamic time-history analysis

In the W-VBI analysis the dynamic response of deck and vehicles is coupled through tyre-pavement contact forces, with wind forces acting on both (Fig. 1(b)). The time-varying vehicle contact points induce dynamic actions on the bridge additional to the wind excitation. Assuming no wheel loss of contact, the bridge response decomposes into single degree-of-freedom (DOF) systems representing relevant vibration modes. The coupled system of dynamics is defined from the displacement vector of the bridge ($\mathbf{q}_b$ in modal coordinates) and the vehicles ($\mathbf{q}_v$), as well as their time-derivatives ($\dot{\mathbf{q}}$, $\ddot{\mathbf{q}}$):

$$\begin{bmatrix} \mathbf{M}_b & \mathbf{0} \\ \mathbf{0} & \mathbf{M}_v \end{bmatrix} \begin{bmatrix} \ddot{\mathbf{q}}_b \\ \ddot{\mathbf{q}}_v \end{bmatrix} + \begin{bmatrix} \mathbf{C}_b & \mathbf{0} \\ \mathbf{0} & \mathbf{C}_v \end{bmatrix} \begin{bmatrix} \dot{\mathbf{q}}_b \\ \dot{\mathbf{q}}_v \end{bmatrix} + \begin{bmatrix} \mathbf{K}_b & \mathbf{0} \\ \mathbf{0} & \mathbf{K}_v \end{bmatrix} \begin{bmatrix} \mathbf{q}_b \\ \mathbf{q}_v \end{bmatrix} = \begin{bmatrix} \mathbf{\Phi}^{\mathrm{T}}(\mathbf{f}_{b,r} + \mathbf{f}_{b,w}) \\ \mathbf{f}_{v,g} + \mathbf{f}_{v,r} + \mathbf{f}_{v,w} \end{bmatrix}, \tag{2}$$

where $\mathbf{M}_l$, $\mathbf{C}_l$ and $\mathbf{K}_l$ are constant mass, damping and stiffness matrices for bridge ($l = b$) and vehicles ($l = v$). The forcing vector from moving wheel-pavement contact includes pavement irregularity effects on vehicle ($\mathbf{f}_{v,r}$) and bridge ($\mathbf{f}_{b,r}$), obtained at each time-step by imposing road displacement profiles at instantaneous contact points. $\mathbf{f}_{v,g}$ represents vehicle gravity forces, and $\mathbf{f}_{v,w}$ steady aerodynamic forces and moments:

$$f_{v,w}^{i} = \frac{1}{2}\rho U_r^2 C_i(\psi) A_f, \quad f_{v,w}^{j} = \frac{1}{2}\rho U_r^2 C_j(\psi) A_f h_v, \tag{3}$$

where ρ is the density of the air; A_f and h_v are the reference surface of the vehicle and the distance between its centroid and the centroid of the deck (see Fig. 1(b)), respectively.

The static coefficients C_i are related to the drag, side and lift forces on the vehicles $f^i_{v,w}$ ($i = D, S, L$, respectively), and C_j refer to the yaw, pitch and roll moments $f^j_{v,w}$ ($j = Y, P, R$, respectively). These coefficients are obtained by linear interpolation from wind tunnel testing and they depend on the instantaneous angle of incidence of the wind on the vehicles ($\psi(t)$), following the system of velocities included in Fig. 2(a), and considering as positive the speed of the vehicles driving eastbound (positive-x direction). The wind-vehicle angle of incidence is given as $\psi = \arctan\left(u^y/(u^x - V_d)\right)$, in which V_d is the driving speed and U is the mean wind speed, which is projected in the along-drive wind ($u^x = U\cos(\beta)$) and the across-drive wind ($u^y = U\sin(\beta)$), where β is the apparent incidence angle of the wind. The resultant wind velocity acting on the vehicle is $U_r^2 = (u^x - V_d)^2 + (u^y)^2$.

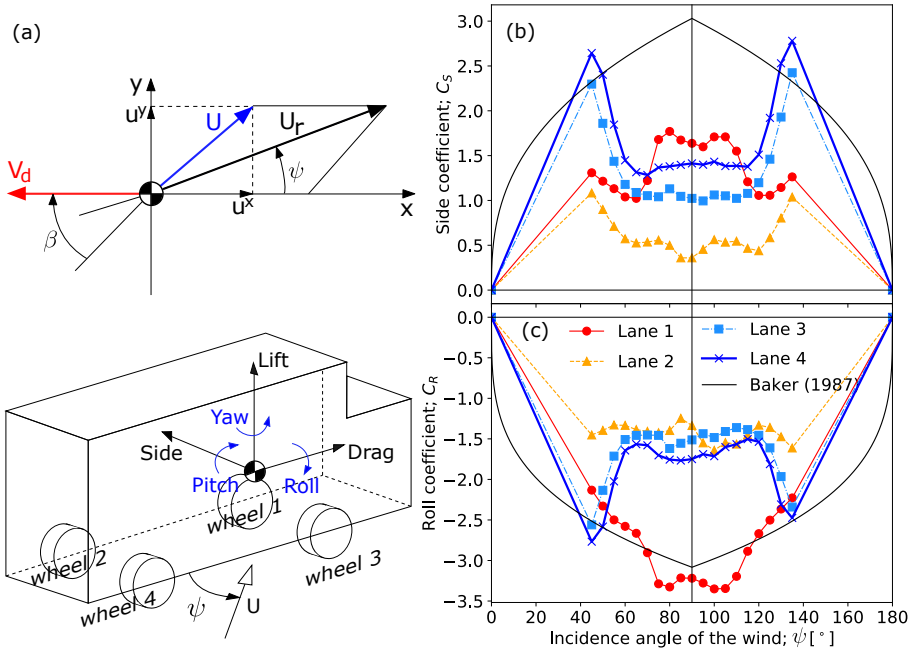

Figure 2: (a) Relative wind/driving velocity system in the case of headwinds, wheel numbering and positive convention of important vehicle aerodynamic coefficients. (b) Time-averaged side and (c) rolling aerodynamic coefficients in the vehicle located on different lanes of the bridge considered. The corresponding off-bridge vehicle coefficients given by Baker (1987) [28] are also included for reference.

The wind force vector on the deck $\mathbf{f}_{b,w}$ is applied to a simplified 3-DOF model of the cross-sections along its length, as shown in Fig. 1(b). In this model $\mathbf{f}_{b,w} = [f^D_{b,w}, f^L_{b,w}, f^M_{b,w}]^{\mathrm{T}}$ represents a vector with the drag, lift and moment components of the wind forcing at each node of the deck, respectively, and $\mathbf{q}_b = [p, h, \alpha]^{\mathrm{T}}$ are the corresponding generalised movements. The deck wind forces are obtained as a linear superposition of the mean,

buffeting and self-excited forces, that is, $\boldsymbol{f}_{b,w} = \boldsymbol{f}_{b,w-s} + \boldsymbol{f}_{b,w-b} + \boldsymbol{f}_{b,w-se}$ [29, 30]. The mean wind forces are given as follows:

$$f^{D}_{b,w-s} = \frac{1}{2}\rho U^2 B C_D, \quad f^{L}_{b,w-s} = \frac{1}{2}\rho U^2 B C_L, \quad f^{M}_{b,w-s} = \frac{1}{2}\rho U^2 B^2 C_M, \tag{4}$$

where B is the depth of the bridge deck; $C_D = C_D(\alpha_s)$, $C_L = C_L(\alpha_s)$ and $C_M = C_M(\alpha_s)$ are the static coefficients of the deck at the angle of attack α_s formed between the mean wind velocity vector and the deck section in static equilibrium.

For simplicity, the buffeting and aeroelastic wind actions in the bridge are obtained with the linear quasi-steady (LQS) model [31] in which the fluid memory is neglected, and with it the aerodynamic admittance. This would effectively increase the buffeting forces in the deck but it can be accepted because it has been demonstrated that the choice of the wind load model in the deck is almost irrelevant in W-VBI analyses at wind speeds significantly lower than the structural design ones [9], such as those conducted for the driving safety assessment in this work. The reader is referred to [3] for a full description of the buffeting ($\boldsymbol{f}_{b,w-b}$) and the aeroelastic ($\boldsymbol{f}_{b,w-se}$) deck forces in the LQS model.

The W-VBI analysis is repeated for each of the N_r records of wind time-histories and pavement profiles simulated in *Step 1* of the analysis.

Step 3: Accident analysis, performance ratios η

This step of the W-VBI framework (Fig. 1(c)) involves *post-processing* of the time-history results obtained in *Step 2* for each wind/pavement realisation. The safety analysis computes the arithmetic mean and the standard deviation (σ) of performance ratios (η).

The driving accident risks are assessed from the time-histories of the vehicle wheel reactions in the vertical and the transverse directions: $F_{c,Z-wh}(t^*)$ and $F_{c,Y-wh}(t^*)$, respectively. Considering the 4-wheel high-sided light truck in Figure 2(a) with wheel numbers $wh = 1, \cdots, 4$, the total forces in the leeward and windward vehicle wheels are defined as $F_{c,Z-L} = F_{c,Z-1} + F_{c,Z-2}$, $F_{c,Z-W} = F_{c,Z-3} + F_{c,Z-4}$, respectively. The total force in the front and real axles of the vehicle are $F_{c,i-F} = F_{c,i-1} + F_{c,i-3}$ and $F_{c,i-R} = F_{c,i-2} + F_{c,i-4}$,

respectively, where $i = Y, Z$ denotes lateral and vertical directions.

The safety against different types of wind-induced vehicle accidents is expressed as:

$$\eta_o = \max_t \left[\frac{F_{c,Z-L}(t) - F_{c,Z-W}(t)}{F_{c,Z-L}(t) + F_{c,Z-W}(t)} \right] \tag{5a}$$

$$\eta_s = \max_t \left[\frac{|f^S_{v,w}(t)|}{\mu_c (F_{c,Z-F}(t) + F_{c,Z-R}(t))} \right] \tag{5b}$$

$$\eta_y = \max \left[\max_t \left(\frac{|F_{c,Y-F}(t)|}{\mu_c F_{c,Z-F}(t)} \right), \max_t \left(\frac{|F_{c,Y-R}(t)|}{\mu_c F_{c,Z-R}(t)} \right) \right], \tag{5c}$$

in which μ_c is the tyre-pavement friction coefficient. Values of η_o, η_s and η_y above 1 indicate that the corresponding limit state has been exceeded, namely overturning, side-slipping, and yawing instability, respectively. In particular, $\eta_o > 1$ implies unloading of the windward wheel line, whereas $\eta_s > 1$ and $\eta_y > 1$ indicate that the lateral tyre force demand of the wheel axles exceeds the available friction resistance [3, 32, 33]. A global accident ratio is also defined as $\eta_G = \max(\eta_o, \eta_s, \eta_y)$ in this study.

Step 4: Skew-dependent critical wind curves and response statistics

For each wind incidence angle and wind speed level, the vehicle driving speed is progressively increased until a driving accident is detected according to the previous accident criteria. This procedure is repeated for all stochastic wind and pavement realisations considered in the analysis, allowing the calculation of a set of critical driving speeds associated with each wind scenario.

From these results, skew-dependent Critical Wind Curves (CWCs) are established, defining the maximum vehicle speed above which accidents may occur for a given wind speed and angle of incidence (Fig. 1(d)). The proposed framework enables the estimation of mean critical wind curves together with their associated statistical dispersion. Details are provided in Section 4.1.

3. Case study

The general W-VBI framework described in Section 2 is next applied to a representative bridge with documented wind-related traffic restrictions. This section introduces the bridge geometry, aerodynamic data, stochastic wind inputs, pavement irregularities, and vehicle properties required for the implementation of the methodology.

3.1. Bridge structure

The proposed methodology is applied to the assessment of the driving safety in the Orwell Bridge (Ipswich, UK). This structure is selected because it has a slender long deck (1287 m) very exposed to wind, with a central span of 190 m. It is located approximately in West-East direction and it holds 4 traffic lanes, two in the North girder (eastbound) and two in the South girder (westbound). Figure 3(a) shows the general arrangement of the bridge in elevation. The deck alignment is straight in plan view, with its centreline contained in the vertical structural plane (SP) used for the wind field definition. The bridge deck consists of two 12-m wide prestressed concrete box girders with variable depth, ranging from 4 m at midspan and at the adjacent spans to 12 m at the central piers (P9 and P10). Figure 3(b) illustrates the cross-sections at these key locations, including the two 1.7-m high edge barriers that extend continuously along the entire length of the deck. The aerodynamic coefficients of the bridge deck were obtained from two-dimensional computational fluid dynamic (CFD) simulations of the wind flow around the bridge deck sections conducted in ANSYS Fluent [34] for angles of attack of the wind ranging from $\alpha_s = -10°$ to $10°$. It should be noted that the present case study focuses on a conventional bridge without towers or other major bluff bodies near the traffic lanes; therefore, local aerodynamic interference effects associated with these elements are outside the scope of this work.

The structure was modeled in the finite element (FE) analysis software ABAQUS [35], using two independent lines of linear-interpolation 3D beam elements for the deck, each connecting the centroids of the box girders. A total of 2,600 elements were used to discretise the deck, with a typical element length of 1 m to accurately capture its depth

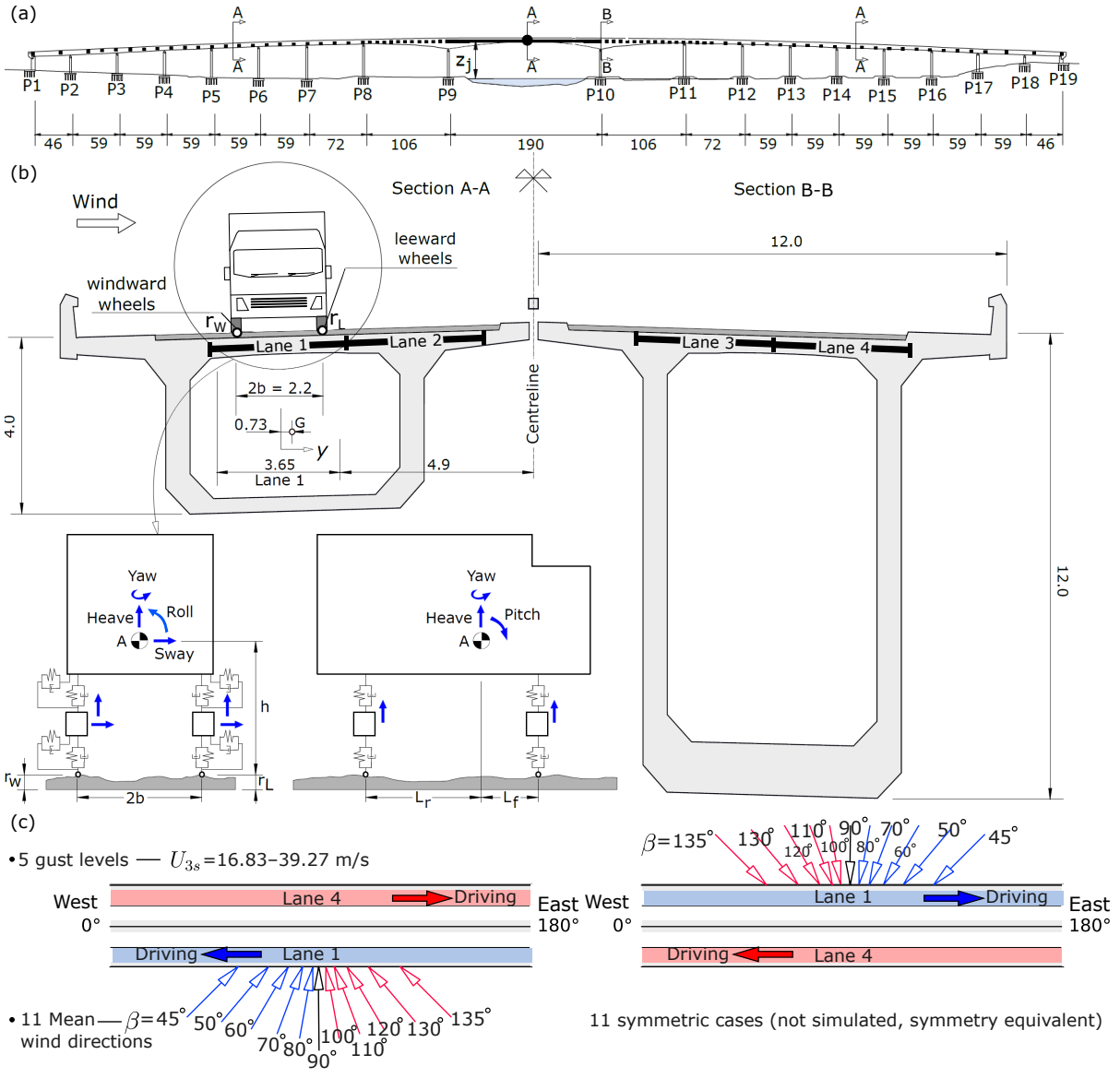

Figure 3: (a) Elevation of the bridge and position of the nodes where wind is generated in $N_p = 110$ nodes. (b) Two relevant cross-sections of the deck and detail of the application of the irregularity profiles (r_W, r_L) to the vehicle wheels, including the numerical model of the latter and its DOF, as well as the transverse distribution of the road lanes. (c) description of the wind cases considered in the study (only 11 representative wind directions are simulated explicitly, the remaining symmetric cases are obtained by equivalence between opposite wind directions and swapped lane positions). Units in meters.

variation. The asphalt layer was accounted for by increasing the concrete density in the deck elements, while the parapets, sidewalks, barriers, and diaphragms were represented as lumped masses located at their respective centroids. The piers were modelled using the same beam element formulation as the deck and were fully fixed at their base. They allow the longitudinal movement of the deck (except P8 to P14) and restrain the lateral one. The resulting FE model of the bridge has approximately 16,000 DOF.

A modal analysis was carried out to identify the vibration modes most relevant to the W-VBI analysis. Fig. 1(a) includes the first vibration mode of interest for the driving safety, which corresponds to a lateral mode of the deck main span and the adjacent spans, between piers P8 and P11, with a frequency of 0.5 Hz. The first vertical vibration mode also involves these spans and it has a frequency of 0.77 Hz. A modal convergence study was performed to determine the number of bridge modes required in the dynamic analysis. Based on this study, only the relevant lateral, vertical, and torsional deck modes up to 5 Hz were retained, while higher-frequency or non-participating modes were excluded due to their negligible influence on the coupled bridge-vehicle response. In total, 74 bridge modes were considered in the W-VBI analysis.

3.2. Turbulent wind field

The wind velocity field is generated at $N_p = 110$ nodes along the deck, and also additional points in the approaching platforms. The position of the N_p points shown in Fig. 3 (a) indicates that the density of generated wind data is higher at the central span, where the mean wind speed is stronger and the movement of the deck is more significant. The wind is only applied on the vehicles and on the deck of the bridge, not on the piers. This is deemed acceptable given the large transverse stiffness of the piers, which can be observed in the first lateral vibration mode included in Fig. 1(a). The height of the deck above ground level at the j-th node (z_j) also varies, reaching a maximum of 48.1 m above the river at the midspan of the central span. This variation is accounted for in the target boundary layer profile when generating the wind field. However, the slope of the deck is not considered in the dynamic response of the vehicle.

A total of $N_r = 100$ independent pseudo-random orthogonal and non-orthogonal wind

velocity signals were obtained at the centreline of the bridge deck. The GP is defined as the vertical plane that forms an angle β with the normal of the SP and intersects with it at the left abutment (P1) if $\beta < 90°$, or at the right abutment (P19) if $\beta > 90°$. The time-step and the frequency band width considered in the wind field generation are Δt = 0.01 s and Δf = 0.001 Hz, respectively. The along-flow mean wind speed profile is defined ignoring orographic effects and considering the specifications of EN1991-1-4 [36] and the UK recommendations [37, 38] for terrain Type II, regardless of the wind incidence angle: $U_j = 0.19\log\left(z_j/0.05\right) U_{z,10}$, with z_j being the height above ground of the j-th deck node, and $U_{z,10}$ the mean along-flow wind speed at the reference height z = 10 m. For practical purposes, the reference mean wind speed is evaluated at the lowest point of the deck (P19, located at z_{19} = 29.5 m), and it is designated as U_b. Hence, $U_{z,10} = 0.82U_b$.

The along-flow turbulence intensity of the j-th node of the deck also depends on z_j, with $I_j^{\widehat{u}} = 1/\log\left(z_j/0.05\right)$, but it is assumed to be invariant with respect to the wind skew angle β. This gives values of $I_j^{\widehat{u}} \approx 0.15$ along the deck of the bridge. Following [39] and assuming homogeneous terrain conditions, the across-flow turbulence intensities are defined as $I_j^{\widehat{v}} = 0.75 I_j^{\widehat{u}} \approx 0.11$ and $I_j^{\widehat{w}} = 0.5 I_j^{\widehat{u}} \approx 0.075$, in the longitudinal and vertical directions, respectively. The along-flow turbulence length scale is estimated in accordance with EN 1991-1-4 [36] as $L^{\widehat{u}}$ = 139 m. The turbulence length scales in the longitudinal and vertical directions are derived as $L^{\widehat{v}} = 0.25 L^{\widehat{u}} \approx 34.75$ m, and $L^{\widehat{w}} = 0.1 L^{\widehat{u}} \approx 13.9$ m. With these parameters, the Kaimal spectra describes the frequency content of turbulence in the i-th direction ($i = \widehat{u}, \widehat{v}, \widehat{w}$) and the j-th node of the GP as:

$$\frac{f\widehat{G}_{jj}^{i}(f)}{(\sigma_j^i)^2} = \frac{A^i \tilde{f}^i}{(1 + 1.5A^i \tilde{f}^i)^{5/3}}, \tag{6}$$

where $\sigma_j^i = I_j^i U_j$ is the standard deviation of the turbulence, defined from the reduced frequency $\tilde{f} = fL^i/U_j$, with the spectral parameters $A^{\widehat{u}} = 6.8$ and $A^{\widehat{v}} = A^{\widehat{w}} = 9.4$.

In the wind generation the spatial coherence decrements for wind turbulence at the bridge site are adopted from [40] as $C_{\widehat{x}}^{\widehat{u}} = C_{\widehat{z}}^{\widehat{u}} = 10$, $C_{\widehat{x}}^{\widehat{v}} = C_{\widehat{z}}^{\widehat{v}} = 6.5$, and $C_{\widehat{x}}^{\widehat{w}} = 6.5$ and $C_{\widehat{z}}^{\widehat{w}} = 3$ for the along-flow, across-flow and vertical turbulent components, respectively.

The dynamic driving stability analysis presented later is based on the 3-s gust along-

flow wind speed calculated from the velocity wind histories at any point j when $\beta = 90°$: $U_{3s,j}$. It has been verified that this value does not change significantly along the deck but, to be conservative, the minimum peak 3-s gust wind speed recorded in its entire length is used to assess the driving safety: $U_{3s} = \min_j(U_{3s,j})$. The 3-s gust factor is $U_{3s}/U_b \approx 1.25$ for all the records and mean wind speeds considered.

3.3. Pavement irregularity surfaces

A total of $N_r = 100$ representative pavement irregularity profiles are generated in compliance with ISO 8608 standards [26], adopting Category A for the analysis. Fig. 3(b) shows the bridge's four-lane configuration across its two box girders, along with the location of a high-sided vehicle centered on the two lanes considered; Lanes 1 (westbound direction) and 4 (eastbound direction). These were selected based on their increased wind-driving accident risks given that the inner lanes (2 and 3) are more shielded from the wind [41]. Due to the lack of lane-specific pavement data, uniform irregularity profiles are assumed in both road lanes. Fig. 3(b) indicates the position of the pavement irregularities in the two wheel lines of the vehicle.

In the random pavement irregularity generation, the target displacement PSD function is $G_d(n_0) = 16 \times 10^{-6}$ m^3/cycle at the reference frequency $n_0 = 0.1$ cycles/m, which corresponds to a very good quality (Road Category A in [26]). The pavement spatial frequency ranges from $n_1 = 6.3 \times 10^{-4}$ cycles/m (lower bound) to $n_N = 20$ cycles/m (upper bound), with $\Delta n = 1.0 \times 10^{-4}$ cycles/m being the frequency resolution.

The pavement profiles are separated transversely by a distance corresponding to the vehicle width: $2b = 2.2$ m. The pavement profiles extend 250 m west of the bridge to allow for the vehicle dynamics to stabilise before entering the deck. A 50-m extension is added to the east to keep consistent conditions in the vehicles after leaving the bridge. A representative pair of independently generated irregularity profiles at both wheel lines is included Fig. 4.

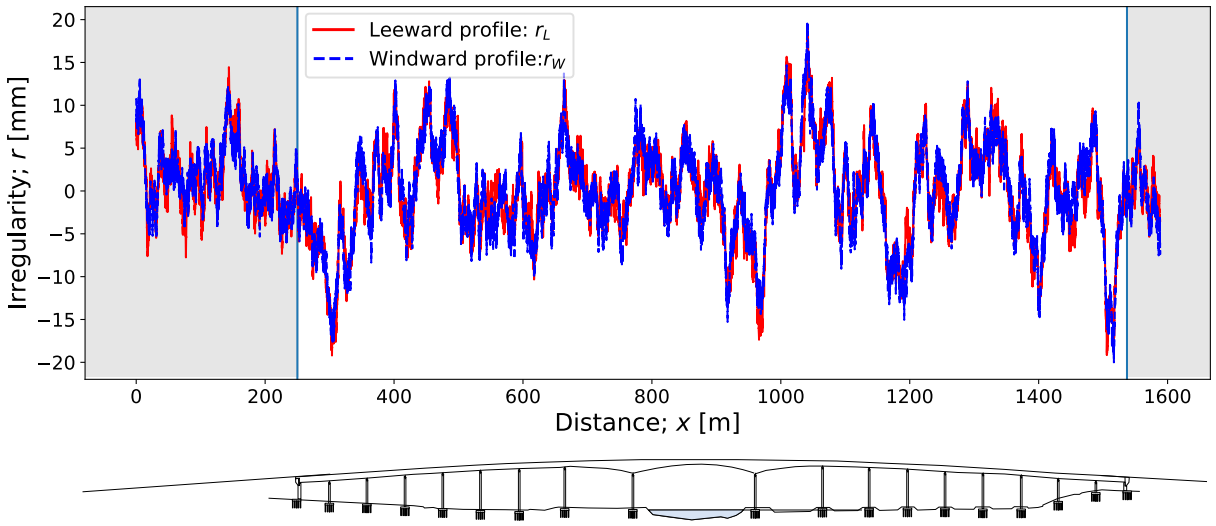

Figure 4: Pavement irregularity profiles along the bridge length in the windward and the leeward wheels. The shaded areas indicate the approaching platforms. Realisation 1.

3.4. High-sided vehicle models

A single unladen high-sided vehicle crossing the bridge at a constant speed V_d centered on Lanes 1 or 4 of the deck is considered in this work. These outermost lanes are the most exposed to crosswind effects and therefore represent the critical traffic positions for safety assessment [41]. A single-vehicle scenario is adopted to isolate wind-induced vehicle instability (e.g. [6, 8, 9]), as traffic-induced deck vibrations are comparatively small for the bridge studied and more complex traffic scenarios would significantly increase computational cost with limited influence on the results. The vehicle is modelled as a 13-DOF system represented in Fig. 3(b), which includes heave, sway, roll, pitch and yaw of the vehicle box, and vertical and lateral displacements of its four wheel/suspension masses. Two different vehicles have been considered in this study from a review of published works [32, 33, 42]. Their mechanical properties are included in Table 1.

Although these two vehicles have different mechanical properties and dimensions, they are assumed to have comparable aerodynamic shapes. Therefore, the same aerodynamic coefficients (C_i, C_j) for different relative wind incidence angles ψ obtained from wind tunnel tests reported in [41] are adopted for both vehicles. Fig. 2 shows the resulting side and rolling coefficients, time-averaged during the experimental testing. This modelling choice allows the influence of moderate variations in representative vehicle parameters to be isolated and assessed within the W–VBI framework, in which stochasticity is introduced

Parameter	**Units**	**Vehicle 1**	**Vehicle 2**
Full length of the vehicle	m	10.82	8.5
Longit. distance from centroid to front wheels	m	2.6	1.74
Longit. distance from centroid to rear wheels	m	3.0	2.96
Reference area (A_f)	m^2	8.68	7.5
Vertical distance between wheels and centroid (h)	m	1.0	1.0
Half distance between wheel lines (b)	m	1.1	1.0
Mass of the vehicle body	kg	4480	6500
Pitching moment of inertia of vehicle body	$kg{\cdot}m^2$	5516	9550
Rolling moment of inertia of vehicle body	$kg{\cdot}m^2$	1349	3030
Yawing moment of inertia of vehicle body	$kg{\cdot}m^2$	10000	100000
Mass of each wheel in front axle	kg	800	400
Mass of each wheel in rear axle	kg	710	400
Upper vertical spring stiffness (all wheels)	kN/m	399	250
Upper lateral spring stiffness (all wheels)	kN/m	299	187.5
Upper vertical damper damping coeff. in front wheels	kN·s/m	23.21	2.5
Upper lateral damper damping coeff. in front wheels	kN·s/m	23.21	2.5
Upper vertical damper damping coeff. in rear wheels	kN·s/m	5.18	2.5
Upper lateral damper damping coeff. in rear wheels	kN·s/m	5.18	2.5
Lower vertical spring stiffness (all wheels)	kN/m	351	175
Lower lateral spring stiffness (all wheels)	kN/m	121	100
Lower vertical damper damping coefficient (all wheels)	kN·s/m	0.8	1.0
Lower lateral damper damping coefficient (all wheels)	kN·s/m	0.8	1.0

Table 1: Mechanical properties of the vehicles considered in this study.

only through wind and pavement inputs, and not through the vehicle properties.

The wind velocity histories acting on the vehicle are obtained by linear interpolation between the two nodes of the deck (or the approaching platforms) that are adjacent to the vehicle centroid at each time-step of the analysis. The wind velocity on the vehicle is increased linearly when it is on the west approaching platform, ranging from 0 at the start of the analysis to full wind speed when the front wheels access the deck of the bridge (at this instant the deck is also subject to full wind speed). This is to avoid introducing unrealistic transient dynamic effects on the vehicle.

3.5. Dynamic analysis, accident risk assessment and simplifying assumptions

The solution of the coupled system of dynamics for the bridge and the vehicle is solved in the time-domain using the modal dynamics library MDyn [43], freely available at https://github.com/AlfredoCamaraC/MDyn. A fixed time-step of 0.01 s and a damping ratio $\xi = 1\%$ equal for all the vibration modes considered in the analysis.

For each of the five 3-s gust wind speed ranging from 16.83 to 39.27 m/s, the vehicle speed is gradually increased until an accident is observed ($\eta_G \geq 1$) to compute the critical driving speed V_c, defined as the maximum safe speed immediately below the accident threshold. This stepwise threshold-search procedure is commonly adopted in previous W-VBI research works [4, 44, 45]. To this end, the sliding-type of accidents are assessed considering a tyre-pavement friction coefficient of $\mu_c = 0.7$, appropriate for dry to moderately wet conditions [46]. The dynamic study considered vehicle speeds that range from 20 to 80 mph (32.19 to 128.75 km/h). In cases where accidents occur at the minimum studied speed of 20 mph (32.19 km/h), the critical speed threshold for accident occurrence is conservatively assigned as $V_c = 0$ km/h, indicating that unsafe conditions are predicted even at the lowest operational speed considered in the analysis. This extrapolation avoids additional low-speed simulations, which have limited influence on wind-induced instability but substantially increased computational time due to longer bridge crossing durations, consistent with previous vehicle safety studies [4, 44]. The results were obtained for each of the $N_r = 100$ wind and pavement records.

The cases with inclined winds only consider situations with headwind (i.e. the wind

reaching the front of the vehicle first) because they are known to be critical for the vehicles' safety, and the same wind records are considered for symmetric cases. For example, the wind records generated for $\beta = 70°$ in Lane 1 are the same as those used for winds with $\beta = 110°$ and the vehicle using Lane 4. This is illustrated in the description of the wind cases in Figure 3(c). In addition, aerodynamic forces are represented using experimental quasi-steady coefficients as functions of wind incidence angle and vehicle position. This widely used approach captures the main directional dependence of aerodynamic loads while neglecting higher-order unsteady effects. Although moving-model wind tunnel techniques have been developed, they remain limited to simplified configurations and are not yet available for the fully coupled stochastic wind–vehicle–bridge interaction problem considered here.

In the present study, uncertainty quantification is focused on the stochastic variability of wind histories and pavement irregularities, while turbulence intensity and vehicle properties are treated deterministically to isolate the influence of record-to-record variability. Other simplifying assumptions involve the definition of the vehicle velocity, which is constant throughout the analysis and follows a straight trajectory without active driver steering corrections. The induced vibrations from other vehicles on the bridge are ignored in the definition of the path of the vehicle. Additionally, the cross-slope of the deck, joint effects at abutments (P1 and P19), and the longitudinal road camber are neglected. These simplifications are consistent with common W-VBI practice and allow the study to focus on the probabilistic influence of stochastic wind and pavement inputs. While additional traffic complexity, driver behaviour, and vehicle interactions may affect quantitative results, they are not expected to alter the general conclusions regarding the importance of record-to-record variability and uncertainty quantification.

4. Results

Fig. 5 shows the wheel reactions of Vehicle 1 as it crosses the bridge under one simulated pavement and orthogonal wind record. The mean wind side force on the vehicle ($\bar{f}^{S}_{v,w}$), shown in Fig. 5(a), increases as the vehicle approaches the main span (between

piers P9 and P10) due to the higher deck elevation, causing the largest peaks in the instantaneous lateral reactions at both axles. The lateral reactions oscillate around this mean force, with larger values at the front axle because the vehicle centroid is located closer to it (see Fig. 3(b)). In contrast, the vertical wheel reactions in Fig. 5(b) contain higher-frequency fluctuations, as they are mainly governed by pavement irregularities rather than wind turbulence. The static front wheel reactions ($F^{\text{static}}_{c,Z-F}$) are larger than the rear ones ($F^{\text{static}}_{c,Z-R}$) due to the centroid position, while the side wind loads the leeward wheels (1 and 2) and unloads the windward wheels (3 and 4). Significant deviations between instantaneous and static wheel reactions are observed in both directions, highlighting the influence of stochastic wind and pavement inputs and the importance of accounting for their randomness.

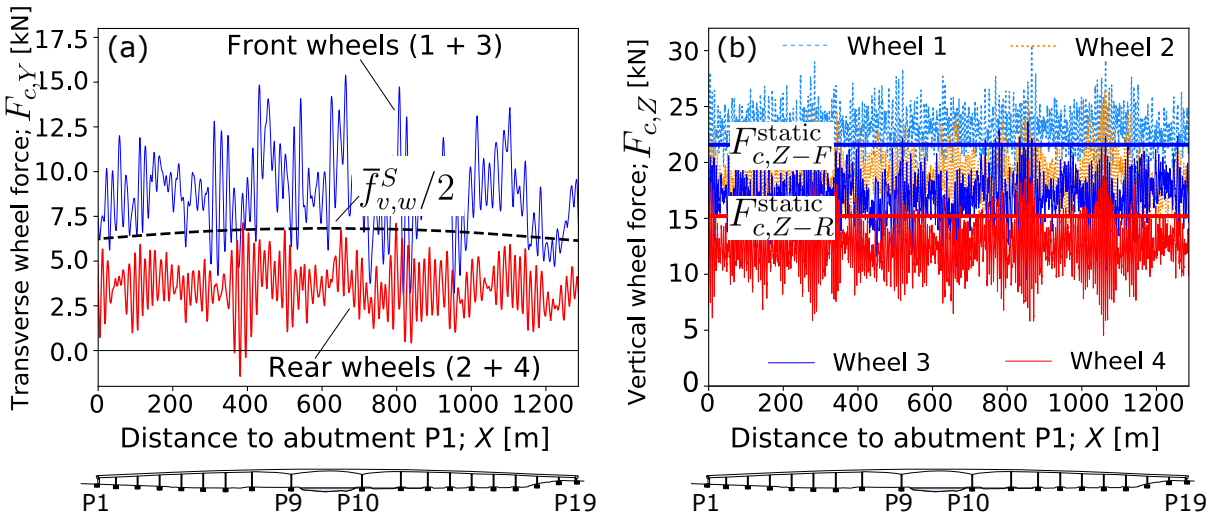

Figure 5: Wheel reactions in the (a) lateral direction, and (b) vertical direction. Pavement and wind velocity realisation 1. Vehicle 1, speed $V_d = 64.4$ km/h. Lane 1. $\beta = 90°$ and $U_{3s} = 22.35$ m/s.

Based on the study of the wheel reactions included in Fig. 5, the analysis of the accident risk ratios in Eq. (5) is presented in Fig. 6. The highest wind-induced vehicle accident risk is recorded at midspan due to the larger value of the side force, as discussed previously. In this case the risk of yawing in the vehicle is higher than side-slipping and overturning, but along the entire deck it is seen that $\eta < 1$, indicating that accidents are not observed for this specific combination of vehicle speed, wind intensity, angle of incidence and pavement irregularity - turbulence record.

It is noted that the results in Figs. 5 and 6 correspond to a single realisation of two

stochastic processes: turbulent wind and pavement irregularities. Therefore, the analysis was repeated for $N_r = 100$ records. For each wind scenario and road lane, the vehicle speed was gradually increased to determine the corresponding critical driving speed (V_c). In total, more than 85,000 dynamic analyses were performed, and the results are presented as Critical Wind Curves (CWC), which define the wind and driving speed combinations above which accidents occur. Fig. 7 shows the mean (μ) and standard deviation (σ) of V_c for the most critical lane and wind angle combinations, compared with the current bridge wind protocol. For a conservative comparison, the mean CWC is reduced by two standard deviations, showing that when the full dataset ($N_r = 100$) is used, the CWC remains above the operational limits. In contrast, using only a reduced subset ($N_r = 10$) may classify currently accepted combinations of relatively low 3-s gust speeds (64-72 km/h) and high vehicle speeds as unsafe. Increasing the number of wind and pavement records improves the statistical confidence of the results and increases the safety margin of the current protocol, particularly for wind speeds below 60 mph. In the limiting case of a stationary vehicle ($V_d = 0$ km/h), variability in the critical wind speed arises only from the turbulent wind histories, as pavement irregularities no longer contribute.

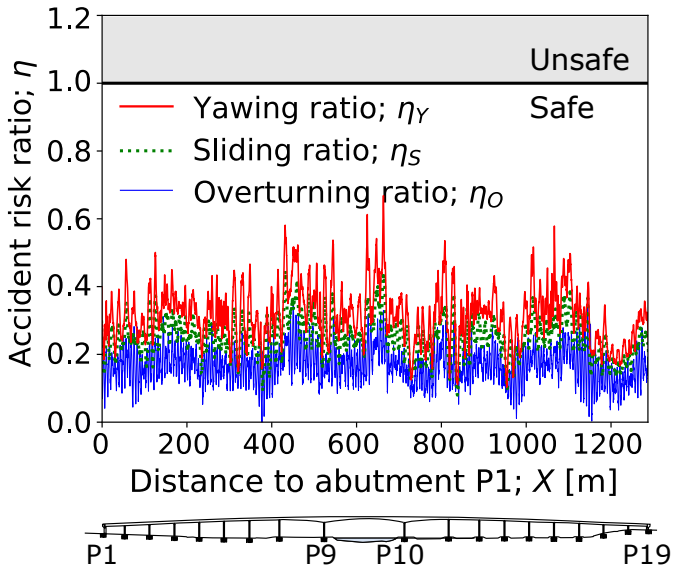

Figure 6: Vehicle 1 accident risk ratios for the pavement and wind velocity realisation 1. Vehicle speed $V_d = 64.4$ km/h. Lane 1. Orthogonal wind ($\beta = 90°$) with $U_{3s} = 22.35$ m/s.

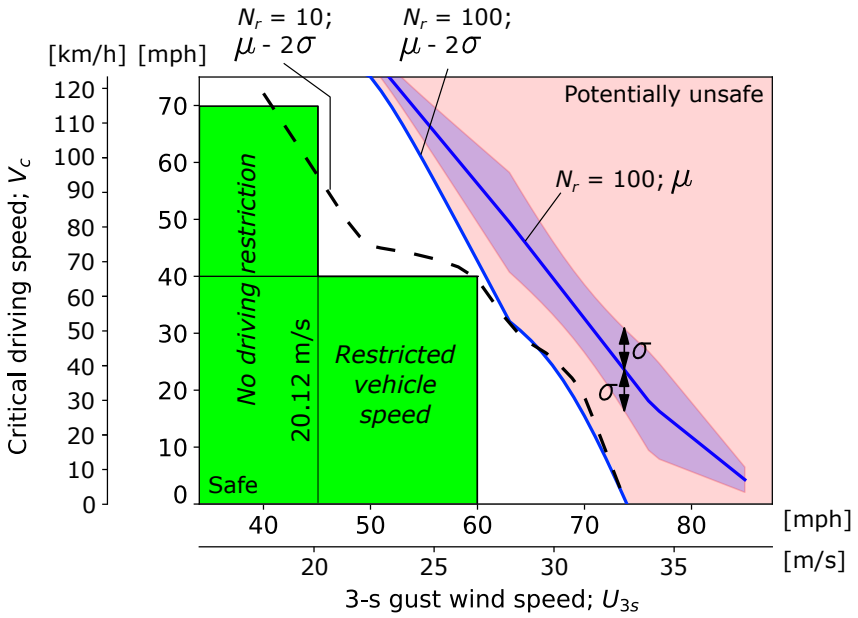

Figure 7: Critical Wind Curve (CWC) for the worst wind incidence angle and lane in each case, obtained for the mean critical driving speed (μ) minus two standard deviations (2σ). The current wind operation protocol of the bridge is included in green. Vehicle 1.

4.1. Influence of the record-to-record variability

The previous result illustrates the importance of the number of wind and pavement records included in the driving safety analysis, this section further explores the degree of confidence associated with the average CWC as N_r increases. Given that the probability distribution of the performance ratios is unknown, bootstrapping techniques were used in this study. To this end, the critical driving speed V_c obtained from the W-VBI analysis of each record is included in the sample vector $\boldsymbol{V_c} = [V_{c,1}, V_{c,2}, \cdots, V_{c,100}]$. A total of N_r results are randomly selected with replacement from $\boldsymbol{V_c}$ to obtain a bootstrap sample $\boldsymbol{V_c}^* = [V^*_{c,1}, V^*_{c,2}, \cdots, V^*_{c,N_r}]$, with $N_r \leq 100$. Each observed performance ratio in $\boldsymbol{\eta}$ has the same probability of being selected for $\boldsymbol{V_c}^*$ (in this case 1/100). The process is repeated 1000 times to obtain relatively smooth and stable confidence intervals [47]. The mean value of the performance ratios in the B_r-bootstrap sample $\boldsymbol{V_c}^*$ (with $B_r = 1, \cdots, 1000$) was computed for each size of the sample $N_r = 1, \cdots, 100$. This mean is referred to as the B_r-bootstrap replication and its 1000 random values for different N_r are included in Fig. 8, in which only three representative gust wind levels are shown, as the two lowest wind cases (U_{3s} = 16.83 and 22.21 m/s) do not generally produce vehicle accidents. The plots in this figure show that the bootstrap replications tend to oscillate about the

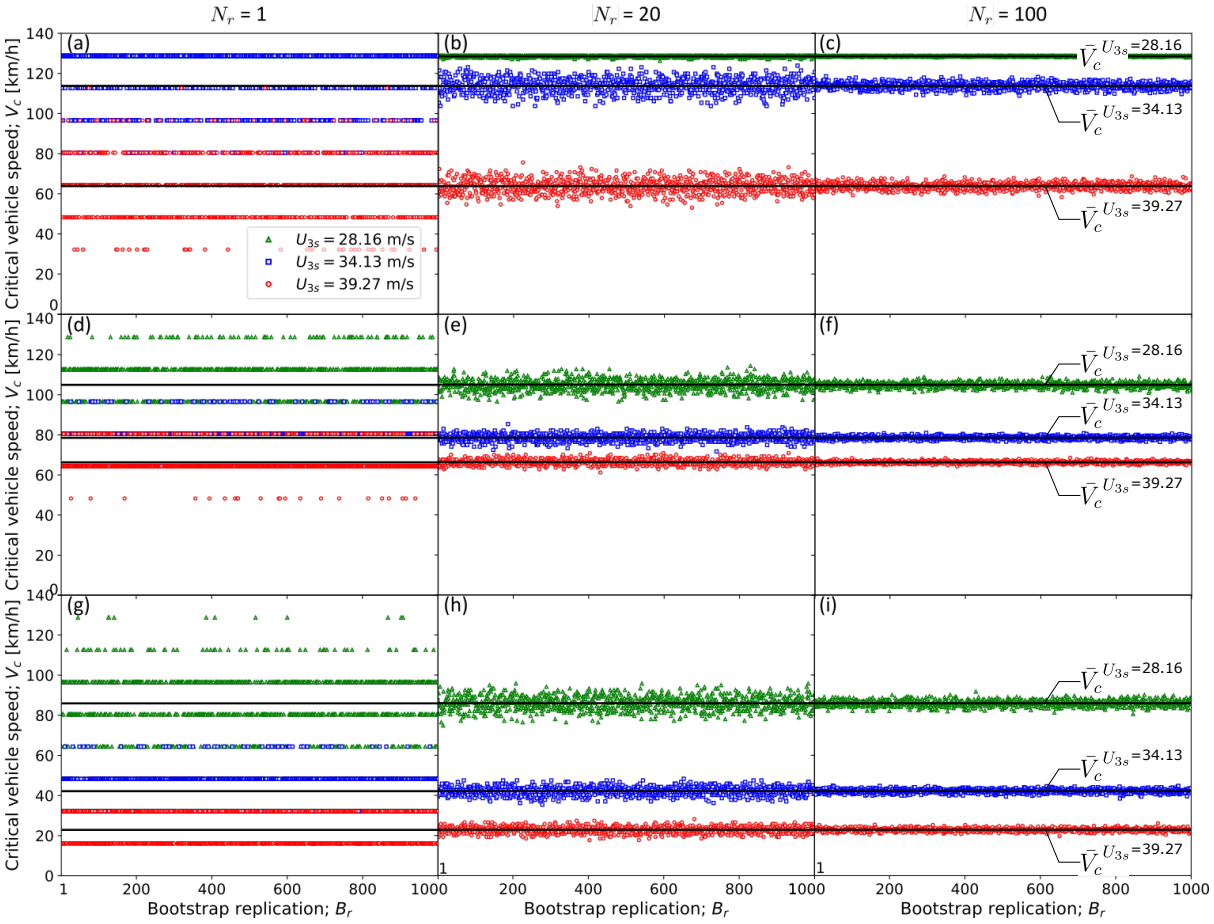

Figure 8: Random realisations of the critical vehicle speed in bootstrap samples of different size (number of records N_r): (a,b,c) skew wind with $\beta = 70°$ in Lane 1 and (a) $N_r = 1$, (b) $N_r = 20$, (c) $N_r = 100$; (d,e,f) orthogonal wind with $\beta = 90°$ in Lane 4 and (d) $N_r = 1$, (e) $N_r = 20$, (f) $N_r = 100$; (g,h,i) skew wind with $\beta = 110°$ in Lane 4 and (g) $N_r = 1$, (h) $N_r = 20$, (i) $N_r = 100$. Vehicle 1.

mean value of the original 100-record sample $\boldsymbol{V_c}$, referred to as $\bar{V}_c^{U_{3s}}$. However, there is a significant variability of V_c for small N_r, particularly for wind speeds of intermediate intensity ($U_{3s} = 34.13$ m/s) because lower or higher wind speeds are more clearly safe or unsafe for vehicles, and there is less scatter in V_c for those situations.

Fig. 9 shows the variability of the mean of the critical driving speed obtained from 1000 bootstrap samples of increasing size N_r, with three different levels of the wind intensity, and two different wind incidence angles. The central lines represent the mean ($\bar{V}_c^*$) of all the 1000 random bootstrap replications of V_c, for each N_r. The upper and lower lines around them are the 2.5$^{\text{th}}$ and the 97.5$^{\text{th}}$-percentiles of the bootstrap distribution: $V_c^{*(2.5\%)}$ and $V_c^{*(97.5\%)}$, respectively (meaning that 2.5 and 97.5% of the samples have a critical driving speed below those two bounds). The range between both limits represents the 95%-confidence interval of the mean critical driving speed: $W_{95} = V_c^{*(97.5\%)} - V_c^{*(2.5\%)}$.

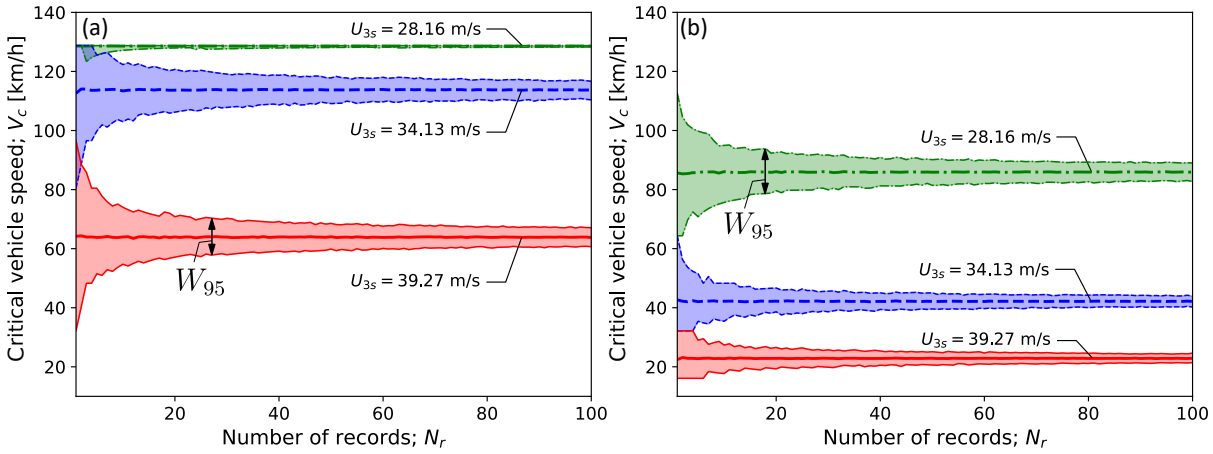

Figure 9: Mean critical wind speed V_c and 95%-confidence intervals represented as shaded bands around the mean: (a) skew wind with $\beta = 70°$ in Lane 1, (b) skew wind with $\beta = 110°$ in Lane 4. Vehicle 1.

The value of $\bar{V}_c^*$ is almost independent of N_r, for all the wind speeds, incidence angles and road lanes considered. However, the width of the confidence intervals decreases significantly by increasing N_r, particularly from 1 to 20 records in cases where accidents are possible (ignoring situations of low speed). Considering a single record, there is a 95%-confidence that the critical driving speed falls between $V_c = 64$ and 111 km/h (i.e. $W_{95} = 47$ km/h) for the case with skew headwinds $\beta = 110°$ and $U_{3s} = 28.16$ m/s. However, for the same wind scenario and considering the average of 20 records, in 95% of the simulations the results will be between $V_c = 78$ and 95 km/h (i.e. $W_{95} = 17$ km/h).

The position of the mean value with respect to the confidence interval limits in Fig. 9 also gives information about the probability distribution. Bootstrap samples composed of small number of records ($N_r = 1$ in the limit) can lead to very non-normal distributions, with the mean value $\bar{V}_c^*$ closer to the 2.5$^{\text{th}}$- or to the 97.5$^{\text{th}}$-percentile, particularly in the case with $U_{3s} = 34.13$ m/s. This supports the use of bootstrapping techniques to obtain W_{95} instead of standard normal distribution tables [47]. In agreement with the central limit theorem, as N_r increases the mean becomes centered between confidence intervals, and the results are closer to a normal probability distribution.

The width of the 95%-confidence interval is normalised to facilitate the comparison between the critical driving speed obtained for different wind scenarios:

$$\widehat{W}_{95} = \frac{W_{95}}{\bar{V}_c^*} = \frac{V_c^{*(97.5\%)} - V_c^{*(2.5\%)}}{\bar{V}_c^*}. \tag{7}$$

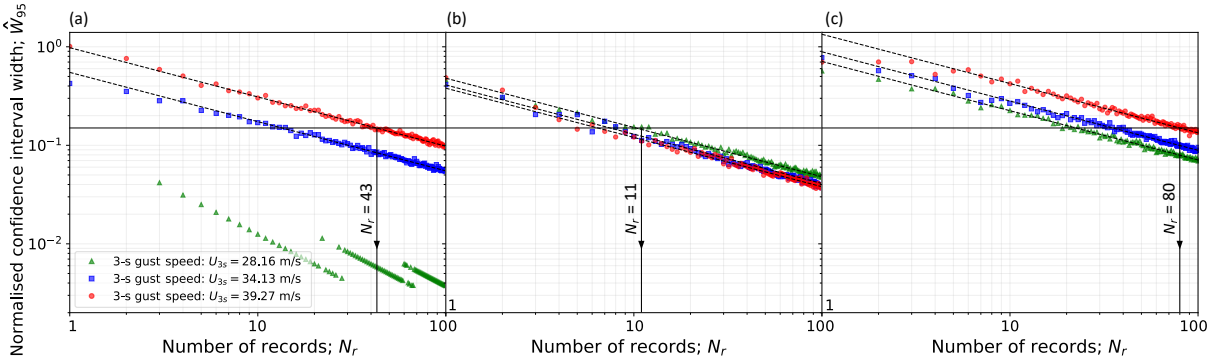

Figure 10: Normalised 95%-confidence interval of V_c in terms of the number of records considered, with: (a) $\beta = 70°$ in Lane 1, (b) $\beta = 90°$ in Lane 4, and $\beta = 110°$ in Lane 4. Vehicle 1.

The values of $\widehat{W}_{95}$ for the critical driving speed are included in Fig. 10 for different wind scenarios. In all the cases with significant driving accident risks, the decrement of $\widehat{W}_{95}$ as N_r increases appear as nearly straight lines in logarithmic coordinates. In order to obtain an analytical expression that predicts such variation, the following model is proposed to fit the obtained data points using least squares (LSQ) minimisation:

$$\log(\widehat{W}_{95}) = \log(a) + b\log(N_r). \tag{8}$$

The results show that $b \approx -0.5$ in all the situations analysed, and therefore:

$$\widehat{W}_{95} = \frac{a}{\sqrt{N_r}}, \tag{9}$$

which has been taken as the LQS model. Fig. 10 shows the good agreement between the results obtained with the fitted Eq. (9) and the data, as well as the minimum number of records required to obtain the critical driving speed with a target confidence of $\widehat{W}_{95}^{\text{target}} = 0.15$. Table 2 gathers the parameter a and the coefficient of determination R^2 of the LSQ fitting (goodness of fit) in all the wind cases considered.

The required number of records strongly depends on the wind speed, incidence angle and road lane, and in general it requires a preliminary bootstrap analysis with the following steps, also illustrated in Fig. 1:

1. run the W-VBI simulation for a reduced number of records: N_r^{test}; recommended at least 5 records in this test to avoid large dispersions in $\widehat{W}_{95}$ (see Fig. 10),

Road Lane 1				Road Lane 4			
β [°]	U_{3s} [m/s]	a	R^2	β [°]	U_{3s} [m/s]	a	R^2
45	28.16	0.27	0.930	90	22.21	0.48	0.987
45	34.13	0.99	0.990	90	28.16	0.41	0.984
50	28.16	0.34	0.979	90	34.13	0.38	0.975
50	34.13	1.19	0.993	100	22.21	0.53	0.985
60	28.16	0.51	0.993	100	28.16	0.60	0.984
60	34.13	1.20	0.993	100	34.13	0.48	0.956
70	28.16	0.55	0.990	110	22.21	0.71	0.992
70	34.13	0.98	0.990	110	28.16	0.89	0.984
80	28.16	0.57	0.990	110	34.13	1.34	0.985
80	34.13	1.74	0.992	120	22.21	0.70	0.986
90	28.16	0.13	0.887	120	28.16	1.12	0.987
90	34.13	3.25	0.990	130	22.21	0.63	0.992
				130	28.16	1.56	0.980
				135	22.21	0.55	0.990
				135	28.16	1.52	0.993

Table 2: Coefficient a and R^2 values for the model $\widehat{W}_{95} = a \times N_r^{-0.5}$. Vehicle 1.

2. do bootstrapping to obtain the width of the 95-% confidence interval for that reduced set of records: $\widehat{W}_{95}|_{N_r^{\text{test}}}$,

3. obtain the number of records required to reach the desired confidence target $\widehat{W}_{95}^{\text{target}}$:

$$N_r = \frac{N_r^{\text{test}} \left(\widehat{W}_{95}|_{N_r^{\text{test}}} \right)^2}{\widehat{W}_{95}^{\text{target}}}. \tag{10}$$

In the following, $N_r = 100$ records is considered, which ensures that $\widehat{W}_{95}|_{N_r^{\text{test}}} < 0.15$ in the most critical cases for the driving stability.

4.2. Influence of the vehicle type and its location across the deck

Fig. 11 compares the CWC obtained with the two high-sided vehicles described in Table 1, for the case with the vehicles using Lane 1 and purely cross-winds ($\beta = 90°$). The results indicate only minor changes in the CWC between both vehicles despite their different mechanical properties, suggesting that for this family of high-sided vehicles the accident risk is governed primarily by aerodynamic loading rather than by variations in vehicle dynamics parameters. Nevertheless, Vehicle 1 is marginally more prone to wind-induced driving accidents due to its lower mass and larger surface, and it is the vehicle

considered hereinafter. It is also observed that with the vehicles crossing the bridge in Lane 1 ($\beta = 90°$) the driving accident risks are moderate due to the shading provided by the upwind parapet. Only for 3-s gust speeds in the order of 35 m/s and above accidents are observed in the vehicles in Lane 1 with purely crosswinds. However, this is not the critical wind scenario and will be discussed later.

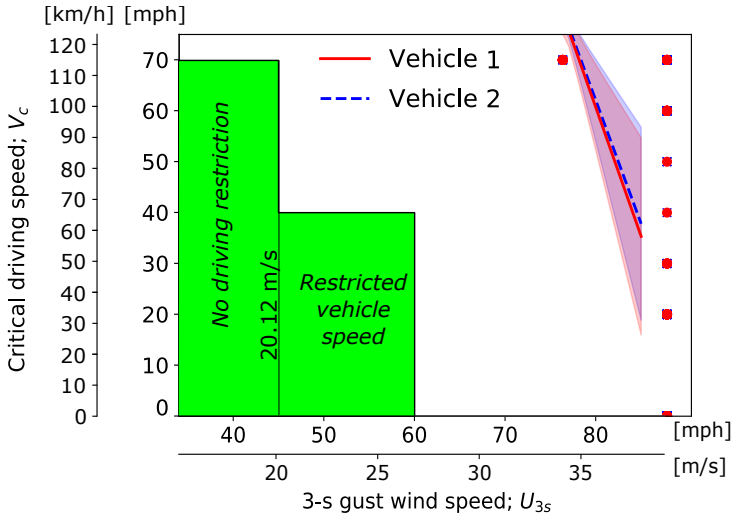

Figure 11: CWC for different types of vehicles. Crosswind ($\beta = 90°$) and vehicles located in Lane 1. The solid lines represent the arithmetic mean of $N_r = 100$ records, and the coloured bands around it have a height of plus/minus one standard deviation. The green shading shows the bridge's wind protocol.

The influence of the road lane in which the vehicle is located is illustrated in Fig. 12 for different wind incidence angles. The downwind lane (i.e. Lane 4) is more prone to vehicle accidents induced by wind, particularly when it is skewed with respect to the deck. This is due to the larger value of the side coefficient in this lane for large skew angles, as shown in Fig. 2(b), which results from the combination of wind flow reattachment and channelling created by the solid bridge parapets along the leeward edge of the deck. However, large rolling aerodynamic coefficients were also measured experimentally in the vehicle located in the windward lane (i.e. Lane 1) for $\beta = 90°$ in Fig. 2(c), which leads to few cases in which purely cross winds and high wind intensities are more detrimental for the safety of the vehicle when it is located in Lane 1 (see Fig. 12(a)).

4.3. Influence of the wind incidence angle

The vehicle accident risks for different wind incidence angles when the driving speed of high-sided vehicles is limited to the current driving speed limits in the bridge ($V_d = 70$

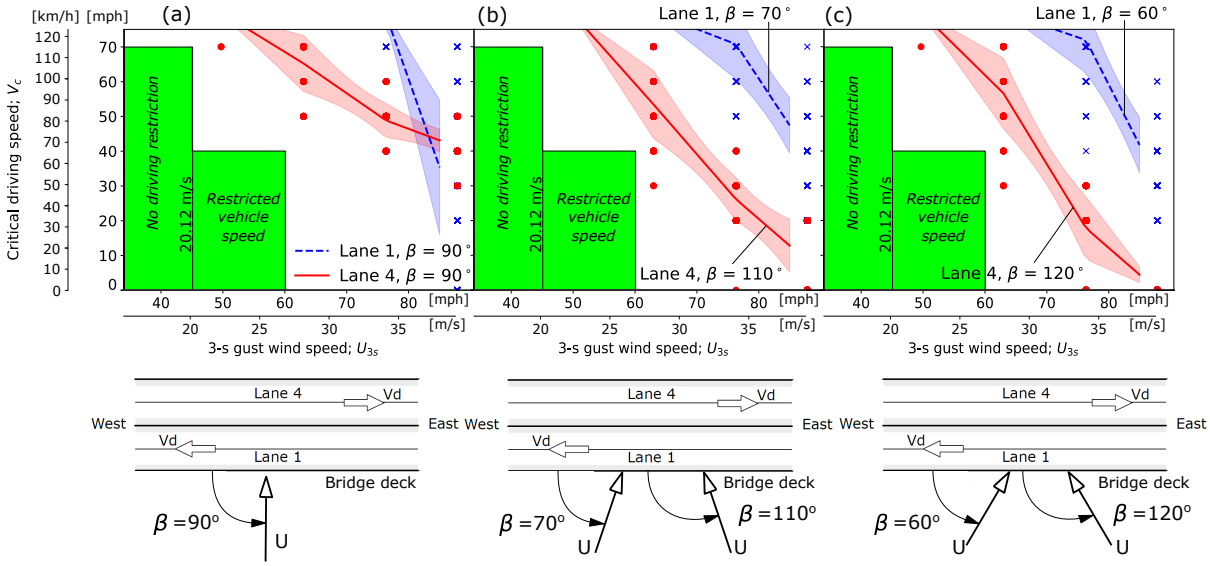

Figure 12: CWC for different lanes with: (a) purely crosswinds ($\beta = 90°$), (b) moderately skewed headwinds ($\beta = 70°$ for Lane 1, and $\beta = 110°$ for Lane 4), and (c) more inclined headwinds ($\beta = 60°$ for Lane 1, and $\beta = 120°$ for Lane 4). Vehicle 1. The solid lines represent the arithmetic mean with $N_r = 100$ records, and the coloured bands around it have a height of plus/minus one standard deviation. The green shading refers to the bridge's wind protocol.

mph and $V_d = 40$ mph) is included in Fig. 13. These are obtained by interpolating from the CWC the wind speed U_c above which accidents occur for a given driving speed, for different values of β to obtain $U_c(\beta)$. Aiming at increasing the confidence in the results, the interpolation is done considering the CWC corresponding to the arithmetic mean minus two standard deviations. Since the results follow a normal distribution given that a sufficiently large number of records is considered ($N_r = 100$), as it was demonstrated in Section 4.1, this would imply that 95.4% of the high-sided vehicles considered would cross the bridge safely if the 3-s gust along-flow wind speed at the level of the deck is below the limits included in the polar plots of Fig. 13. The results show that wind incidence angles coming from the southeast in the range $\beta = 110° - 135°$ are critical because they can trigger vehicle accidents on Lane 4 (leeward lane). This is directly related to the strong influence of lane position and wind incidence angle on the local aerodynamic modification of the flow by the deck and parapets. Previous CFD and wind tunnel studies on this bridge [41] showed that the side parapets partially shield vehicles under crosswind conditions, particularly near the deck centre and windward side. Under skew winds, however, the deck induces flow channelling along the bridge axis and local flow reattachment in the downwind girder, which can amplify aerodynamic loads and

rolling moments on vehicles travelling in the leeward lane. This explains the critical conditions observed in the present study for skew headwinds and leeward-lane traffic.

Due to symmetry of the bridge, winds coming from the northwest with $\beta = 290° - 315°$ are also critical for vehicles circulating on Lane 1, which would be the leeward lane in that case as shown in Fig. 3(c). It is observed that a high-sided vehicle crossing the bridge at 40 mph (64.4 km/h) is likely to do it safely if the wind speed is below 60 mph (26.8 m/s), regardless of its orientation, but this wind speed limit could be increased significantly if the wind incidence angle is considered in the operation protocol. However, if the vehicle velocity is 70 mph (112.7 km/h) the critical wind speed above which accidents could occur is reduced to 50 mph (22.4 m/s).

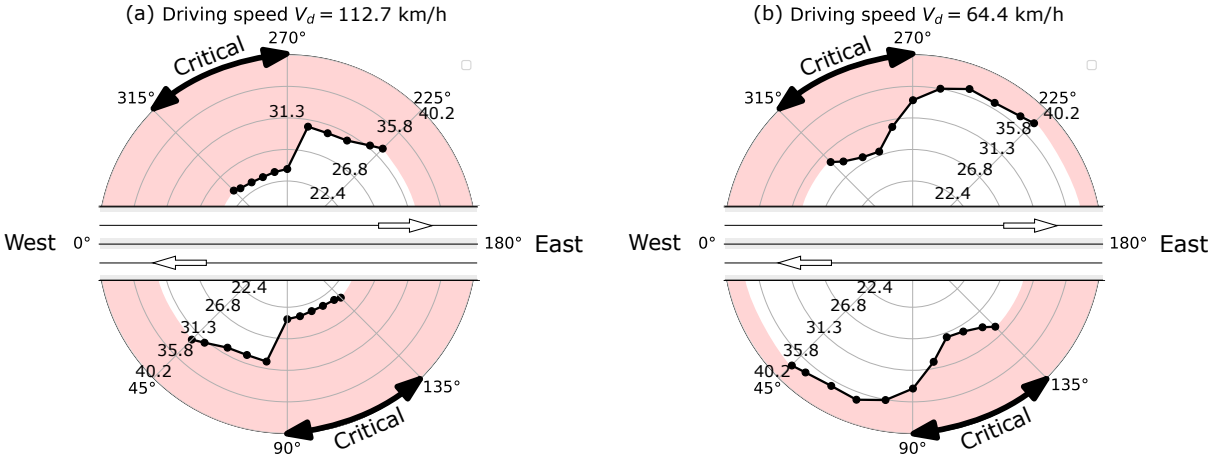

Figure 13: Polar plots with the maximum admissible 3-s wind speed (U_c) in the site of the bridge represented in the radial coordinate (in m/s) with respect to the apparent wind incidence angle (β) in the polar coordinate: (a) driving speed of 70 mph (112.7 km/h), (b) driving speed of 40 mph (64.4 km/h). The red colour shading indicates potentially unsafe wind speeds.

In the site of the bridge the most likely direction of strong winds is southwest, according to the wind rose provided by the meteorological office. This is in principle favourable for the safety of vehicles crossing the bridge according to the results presented in Fig. 13, because southwest winds affect more the vehicles located on Lane 1, and the shape of the deck is able to offer some protection to them as it was observed in the wind tunnel testing. However, there are also records of strong winds from the southeast ($\beta = 110° - 120°$) at the site, and this can be critical for the stability of vehicles in the north girder. At this location, the shape of the deck does not shield the traffic, instead, it generates complex turbulent flow along the deck that could create hazardous conditions for the vehicles.

5. Conclusions

This study proposed a probabilistic W-VBI framework to quantify the record-to-record variability in the wind-induced accident risks on vehicles crossing bridges under stochastic wind and pavement conditions. The main findings are:

- The inherent randomness of the turbulent wind and pavement irregularity affect significantly the safety of the vehicles on the bridge. For specific records of those two stochastic processes a wheel may go through a localised depression of the pavement surface (or a downwards movement of the deck) at the same instant as the vehicle is subject to a wind gust, thereby increasing the risk of accidents.

- The latter observation leads to a large record-to-record variability of the Critical Wind Curve (CWC) in the bridge, and it is important to consider a sufficiently large number of pavement and wind velocity histories to have results with statistical significance.

- A study with bootstrapping techniques determined that the mean value of the driving speed above which accidents occur is almost unaffected by increasing the number of records in the analysis, but the confidence in the results strongly increase and the histograms assimilate more to a normal distribution.

- A simple analytical expression is proposed to estimate the confidence associated with the vehicle safety analysis of bridges using least squares minimisation techniques, which can also be used to calculate the number of records required in the analysis to reach a target confidence in the results.

- For the two representative high-sided vehicles considered, varying mechanical characteristics and exposed area while maintaining the aerodynamic shape did not significantly influence driving safety. This observation is limited to the family of high-sided light goods vehicles considered in this study and should not be directly extrapolated to vehicles with substantially different aerodynamic characteristics.

- The position of the vehicle across the width of the deck, and the wind incidence angle are very important for assessing the risk of accidents. The worst case is usually related to skew headwinds acting on the vehicle located in the leeward lane.

The results highlight the importance of explicitly accounting for stochastic wind and pavement variability in reliability-based traffic management on wind-sensitive bridges. In practical applications, the proposed framework can support the definition of statistically stable safety thresholds and traffic restrictions under adverse wind conditions. However, the quantitative results presented correspond to the selected representative case study and should not be directly extrapolated to all bridge or vehicle types. Nevertheless, the proposed probabilistic framework is general and can be extended to alternative vehicle classes, bridge configurations, aerodynamic deck sections, and wind environments. Future work should extend the methodology to additional vehicle categories, pavement adherence models and traffic scenarios involving multiple vehicles with wind shading effects.

Acknowledgements

This study was commissioned and fully funded by Highways England. Views and opinion expressed are however those of the authors only and do not necessarily reflect those of Highways England, which cannot be held responsible for them.

References

[1] R. Pritchard, "Wind effects on high sided vehicles," *J. Inst. Highw. Transp.*, vol. 56, pp. 22–25, 1985.

[2] A. Camara, C. Jagadeesh, S. Husain, and P. Polec, "Driving stability in the queen elizabeth ii bridge under high winds," in *13th UK Conference on Wind Engineering*, (Leeds (UK)), pp. 171–192, UK Wind Engineering Society, 2018.

[3] A. Camara, "Vehicle–bridge interaction and driving accident risks under skew winds," *Journal of Wind Engineering and Industrial Aerodynamics*, vol. 214, p. 104672, 2021.

[4] A. Camara, I. Kavrakov, K. Nguyen, and G. Morgenthal, "Complete framework of wind-vehicle-bridge interaction with random road surfaces," *Journal of Sound and Vibration*, vol. 458, pp. 197–217, 2019.

[5] C. Cai and S. Chen, "Framework of vehicle-bridge-wind dynamic analysis," *Journal of Wind Engineering and Industrial Aerodynamics*, vol. 92, pp. 579–607, 2004.

[6] Y. Xu and W. Guo, "Dynamic analysis of coupled road vehicle and cable-stayed bridge systems under turbulent wind," *Engineering Structures*, vol. 25, pp. 473–486, 2003.

[7] S. Chen and C. Cai, "Accident assessment of vehicles on long-span bridges in windy environments," *Journal of Wind Engineering and Industrial Aerodynamics*, vol. 92, pp. 991–1024, 2004.

[8] Y. Xu and W. Guo, "Effects of bridge motion and crosswind on ride comfort of road vehicles," *Journal of Wind Engineering and Industrial Aerodynamics*, vol. 92, pp. 641–662, 2004.

[9] I. Kavrakov, A. Camara, and G. Morgenthal, "Influence of aerodynamic model assumptions on the wind-vehicle-bridge interaction," in *IABSE Symposium*, (Stockholm), 2016.

[10] Y. Han, C. Cai, J. Zhang, S. Chen, and X. He, "Effects of aerodynamic parameters on the dynamic responses of road vehicles and bridges under crosswinds," *Journal of Wind Engineering and Industrial Aerodynamics*, vol. 134, pp. 78–95, 2014.

[11] Y. Zhou and S. Chen, "Fully coupled driving safety analysis of moving traffic on long-span bridges subjected to crosswind," *Journal of Wind Engineering and Industrial Aerodynamics*, vol. 143, pp. 1–18, 2015.

[12] W. Guo and Y. Xu, "Safety analysis of moving road vehicles on a long bridge under crosswind," *Journal of Engineering Mechanics*, vol. 132, no. 4, pp. 438–446, 2006.

[13] J. Li, L. Yan, X. He, and T. Lu, "Driving safety assessment of high-sided vehicles on long-span truss suspension bridges subjected to crosswind," *Journal of Wind Engineering and Industrial Aerodynamics*, vol. 268, p. 106287, 2026.

[14] J. Zhang, C. Zhu, and C. Ma, "Driving safety analysis of wind–vehicle–bridge system considering aerodynamic interference," *Journal of Wind Engineering and Industrial Aerodynamics*, vol. 245, p. 105649, 2024.

[15] Y. Liu, S. Chen, Y. Han, and Z. Xiong, "Modularized physics-driven dynamic response prediction of long-span bridge and traffic system subjected to stochastic loads based on neural operators," *Journal of Bridge Engineering*, vol. 30, no. 10, 2025.

[16] J. Hu, G. Lu, W. Zhou, H. Wu, S. Zhang, and C. Miao, "Analysis of dynamic response and driving safety of ultra-high pier long-span rigid-frame bridge under nonstationary wind," *International Journal of Structural Stability and Dynamics*, vol. 26, p. 2650406, 2026.

[17] D. Xia, C. Chen, Y. Hu, Z. Lin, Z. Yuan, and L. Lin, "Computational analysis of wind-induced driving safety under wind–rain coupling effect based on field measurements," *Vehicles*, vol. 7, p. 64, 2025.

[18] Y. Fu, F. Wu, C. Chai, W. Cui, Y. Li, and L. Zhao, "Assessment of driving safety and comfort during vortex-induced vibrations in a long-span bridge considering wind-vehicle-bridge interactions," *Journal of Wind Engineering and Industrial Aerodynamics*, vol. 257, p. 106007, 2025.

[19] H. He and X. Li, "An advanced train-track-bridge coupling analysis method considering vortex-induced vibration of bridge," *Journal of Vibration and Control*, 2026.

[20] T. Wu, W. Qiu, H. Wu, G. Yao, and Z. Guo, "Coupled vibration analysis of ice–wind–vehicle–bridge interaction system," *Journal of Marine Science and Engineering*, vol. 11, no. 3, p. 535, 2023.

[21] J. Shen, Z. Wang, J. Qing, H. Xiang, and Y. Li, "Dynamic response of road vehicle–bridge system under wake-induced vertical vibration of long-span parallel

cable-stayed bridges," *International Journal of Structural Stability and Dynamics*, p. 2750182, 2027.

[22] S. Kim, H.-Y. Cheon, and H.-K. Kim, "A data-driven risk assessment of vehicles traversing long-span sea-crossing bridges accounting for rainfall effect," *Structure and Infrastructure Engineering*, pp. 1160–1172, 2025.

[23] S. Kim, M. Seyedi, and H.-K. Kim, "Risk assessment of wind-induced vehicle accidents on long-span bridges using onsite wind and traffic data," *Journal of Structural Engineering*, vol. 148, no. 10, p. 04022155, 2022.

[24] H. Yang, Z. Jin, K. Chen, and Y. Li, "Extrema estimation of vehicle-bridge interaction responses under crosswind via probabilistic decoupling," *Journal of Wind Engineering and Industrial Aerodynamics*, vol. 270, p. 106353, 2026.

[25] P. S. Veers, "Three-dimensional wind simulation," Tech. Rep. SAND88-0152, UC-261, Sandia National Laboratories, Albuquerque, NM, USA, 1988. Technical Report.

[26] *ISO 8608:1995: Mechanical vibration - Road surface profiles - Reporting of measured data*, 1995.

[27] M. Shinozuka, "Simulation of multivariate and multidimensional random processes," *The Journal of the Acoustical Society of America*, vol. 49, pp. 357–368, 1971.

[28] C. Baker, "Measures to control vehicle movement at exposed sites during windy periods," *Journal of Wind Engineering and Industrial Aerodynamics*, vol. 25, pp. 151–161, 1987.

[29] X. Chen and A. Kareem, "Advances in modeling of aerodynamic forces on bridge decks," *Journal of Engineering Mechanics*, vol. 176, pp. 825–839, 2018.

[30] I. Kavrakov and G. Morgenthal, "A comparative assessment of aerodynamic models for buffeting and flutter of long-span bridges," *Engineering*, vol. 3, pp. 823–838, 2017.

[31] A. Davenport, "The response of slender, line-like structures to a gusty wind," *Proceedings of the Institution of Civil Engineers*, vol. 23, no. 3, pp. 389–408, 1962.

[32] J. Zhu, W. Zhang, and M. Wu, "Evaluation of ride comfort and driving safety for moving vehicles on slender coastal bridges," *Journal of vibration and acoustics*, vol. 140, pp. 051012–1–15, 2018.

[33] N. Chen, Y. Li, B. Wang, Y. Su, and H. Xiang, "Effects of wind barrier on the safety of vehicles driven on bridges," *Journal of wind engineering and industrial aerodynamics*, vol. 143, pp. 113–127, 2015.

[34] A. FLUENT, "Ansys 2019 r1," 2019.

[35] Abaqus, "Finite element analysis program," Providence USA, 2020.

[36] EC1, "Eurocode 1: Actions on structures - part 1-4: General actions - wind actions," 2005. EN 1991-1-4:2005.

[37] *UK National Annex to Eurocode 1: Actions on structures, Part 1-4: General Actions - Wind Actions*, 2010.

[38] *BS6399: Part 2: Loading for buildings: Part 2: Code of practice for wind loads*, 1996.

[39] E. Strommen, *Theory of bridge aerodynamics. Second Edition.* Springer, 2010.

[40] G. Solari and G. Piccardo, "Probabilistic 3-d turbulence modeling for gust buffeting of structures," *Probabilistic Engineering Mechanics*, vol. 16, pp. 73–86, 2001.

[41] A. Camara, L. Fernandez-Elvira, C. Stroumpouli, and C. Jagadeesh, "Skew wind actions on vehicles crossing bridges with solid parapets," *Journal of Wind Engineering and Industrial Aerodynamics*, vol. 240, p. 105485, 2023.

[42] Y. Han, C. Cai, J. Zhang, S. Chen, and X. He, "Effects of aerodynamic parameters on the dynamic responses of road vehicles and bridges under cross winds," *Journal of wind engineering and industrial aerodynamics*, vol. 134, pp. 78–95, 2014.

[43] A. Camara, "A fast mode superposition algorithm and its application to the analysis of bridges under moving loads," *Advances in Engineering Software (currently in press)*, 2020.

[44] D. Zhang and T. Ishihara, "Numerical study of tornado-induced unsteady crosswind response of railway vehicle using multibody dynamic simulations," *Journal of Wind Engineering and Industrial Aerodynamics*, vol. 222, p. 104919, 2022.

[45] M. Batista and M. Perkovic, "A simple static analysis of moving road vehicle under cross wind," *Journal of Wind Engineering and Industrial Aerodynamics*, vol. 128, pp. 105–113, 2014.

[46] Jones and Childers, *Contemporary College Physics*. 3rd ed., 2001.

[47] B. Efron and R. Tibshirani, *An Introduction to the Bootstrap*. chapman & hall, crc, new york (usa) ed., 1993.